Simultaneous Observation of the Er- and Fe-Sublattice Magnetization of Ferrimagnetic $Er_3Fe_5O_{12}$ in High Magnetic Fields Using X-Ray Magnetic Circular Dichroism at the Er $L_{2,3}$ Edges

C. Strohm*
Deutsches Elektronen Synchrotron, Notkestrasse 85, 22607 Hamburg, Germany

P. van der Linden, O. Mathon, and S. Pascarelli
European Synchrotron Radiation Facility, B.P. 220, 38043 Grenoble, France

(Received 8 September 2017; revised manuscript received 3 October 2018; published 28 March 2019)

X-ray magnetic circular dichroism (XMCD) studies at the Er $L_{2,3}$ edges of $Er_3Fe_5O_{12}$ exhibit a change of the spectral shape as a function of temperature and magnetic field. Using singular value decomposition, this variation is understood as a linear combination of two components. The dominating component is associated with the Er magnetization, while the second contribution is identified as an induced signal from the Fe sites. XMCD at either of the L edges in $Er_3Fe_5O_{12}$ provides information on the net magnetization of both sublattices. Their evolution in fields up to 30 T reveals details of the ferrimagnetic interactions on two very different scales.

DOI: 10.1103/PhysRevLett.122.127204

Ferrimagnets play an important role for technology as well as from a fundamental point of view. The rare earth iron garnets (RIGs) were key in the demonstration of molecular field theory [1], later employed in bubble memories, microwave devices, and optical isolators, while the rare earth transition metal intermetallics (RTIs) are used for permanent magnets. Their desirable properties result from details of the exchange between the magnetic constituents and their respective magnetizations. A thorough understanding of their magnetic phase diagram requires one to probe the sublattices independently in fields that are strong enough to compete with their interactions. Many x-ray magnetic circular dichroism (XMCD) studies on ferrimagnets were conducted with the aim of extracting the sublattice magnetizations. A puzzling observation was made when studying the rare earth's (R's) $L_{2,3}$ edges in both the RTIs [2–10] and the RIGs [11–13]: There often is a sizable induced signal from the transition metal (T); i.e., the R L-edge spectra contain information on both the T and the R sublattice, defeating a direct interpretation of XMCD amplitudes and integrals. Different approaches were employed to disentangle the two spectral contributions and to investigate their origin. In some systems, spectral features were directly attributed to the R- or T-sublattice magnetization [3,11,12]. A better understanding was obtained through the subtraction of reference spectra from samples with a nonmagnetic transition metal [2–10]. In the case of the RTIs, a large body of work has established that the $T(3d) - R(5d)$ hybridization is at the origin of the induced contribution [2–10], which closely follows the magnetism of the transition metal, and this finding was ultimately exploited to perform element selective magnetometry at a single absorption edge [14].

Here, we focus on the RIGs, where the interaction due to the ferrimagnetic superexchange via the oxygen $2p$ orbitals is of a different nature. Unlike previous studies, we use singular value decomposition (SVD) for a spectral decomposition of the XMCD signal at the Er $L_{2,3}$ edges, with the goal of isolating the rare earth behavior. We show that the field dependence of the L-edge XMCD from $Er_3Fe_5O_{12}$ is described by two independent parameters. The corresponding spectral components are attributed to the Er and Fe ions, and their field dependence is associated with the sublattice magnetizations. This allows one to study their respective role in the saturation process through XMCD at a single absorption edge.

In the RIGs, the magnetic ions are located at the centers of oxygen polyhedra with different symmetries. The superexchange over the oxygen atoms at their vertices leads to ferrimagnetic interactions with different strength: On one side, the coupling between the two octahedral and three tetrahedral Fe sites is very strong and the antiferromagnetic alignment is broken only at the Curie temperature of 560 K or in excessively high fields. On the other side, the interaction of the Er ions with the unbalanced Fe net moment is much weaker yet still requires applied fields of the order of tens of teslas to compete with the molecular fields. Figure 1 shows a phase diagram, calculated using an isotropic two sublattice model [15]. $Er_3Fe_5O_{12}$ is anisotropic [16], yet this simple toy model contains the essential signatures arising from the weak interaction of the Er ions with the net moment of the ordered Fe sites for fields applied along the easy magnetization axis at temperatures

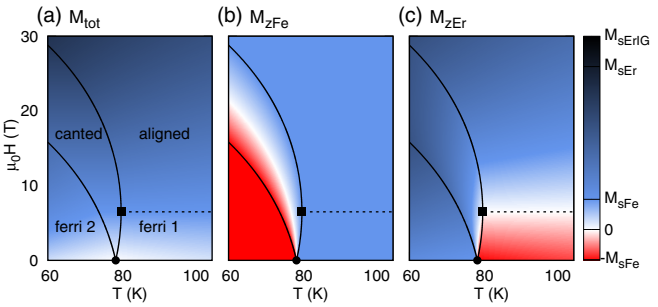

FIG. 1. Isotropic two sublattice toy model for the temperature field phase diagram of $Er_3Fe_5O_{12}$. Filled circle, compensation point; dashed line, field H_m at which the Er sublattice is demagnetized; filled square, T_{crit}, H_m; solid lines, second order transitions bounding the canted phase. (a) total magnetization. (b),(c) Components of the Fe- and Er-sublattice magnetizations along the applied field. The color scale is in units of the sublattice saturation magnetizations $M_{s\mathrm{Fe}}$ and $M_{s\mathrm{Er}}$.

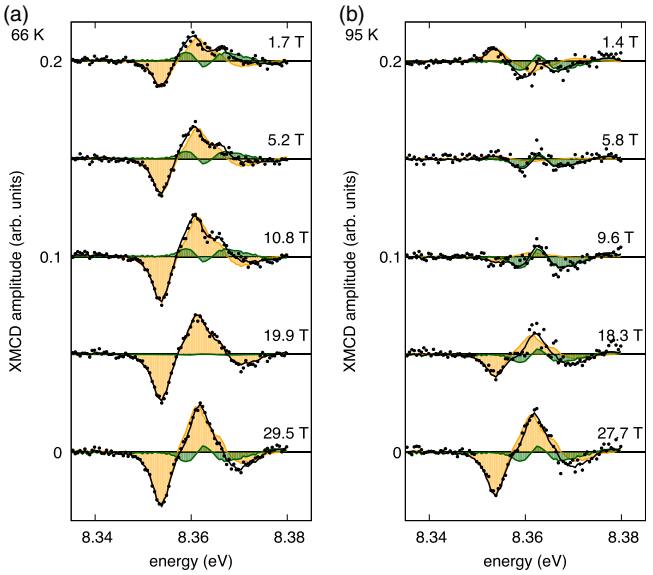

FIG. 2. XMCD at the Er L_3 edge below and above the compensation temperature. (a) 66 K. (b) 95 K. Dots, raw data for selected spectra acquired during the falling part of the field pulse; black line, reconstruction of the data using only the two dominating contributions shown as shaded areas; green, contribution associated with the Fe sublattice; orange, contribution associated with the Er sublattice.

around the compensation point. It comprises two ferrimagnetic regions, a canted phase, and saturation. Outside the upper boundary of the canted phase, the Er sublattice behaves like a paramagnet in the local molecular field H_m of the ordered Fe sublattices, and its magnetization disappears when the latter is compensated for by an applied field (dashed line). Below the critical temperature T_{crit} for the ordering of the Er ions, a canted phase separates the ferrimagnetic regions from saturation. It emerges from the compensation point and is bounded by second order transitions (solid lines). The bulk magnetization [Fig. 1(a)] always rises with the field at all temperatures. Details of the magnetization process including full reversal of the individual components and the different strength of the interactions are expected to be revealed only in the field dependence of the sublattice magnetizations [Figs. 1(b) and 1(c)].

XMCD at the Fe K edge shows, indeed, that the net Fe magnetization in $Er_3Fe_5O_{12}$ is constant outside the canted phase, inside of which it reverses its orientation by 180° through continuous rotation [17]. In order to obtain the full picture, we performed XMCD at the Er $L_{2,3}$ edges in fields up to 30 T with the aim to probe the projection of the Er net magnetization on the applied field along relevant sections of the phase diagram up to saturation.

Transmission experiments at the Er $L_{2,3}$ edges were performed at the energy dispersive x-ray absorption spectroscopy beam line ID24 at the European Synchrotron Radiation Facility [18]. X rays were circularly polarized using a diamond quarter wave plate in a quasinondispersive setting with the polychromator [19]. Fields along the beam up to 30 T were generated by a high duty cycle miniature pulsed magnet [20], and XMCD was detected at fixed polarization while flipping the field. The acquisition of full energy spectra at different field values is key for the subsequent analysis using SVD. In the present pulsed field experiments, this was achieved through use of a multiframe detection scheme [21] at the energy dispersive beam line ID24 [18]. The sample was oriented along the 100 direction, cut, polished, and sandwiched as a freestanding platelet between two Si substrates with holes of 500 μm for the x-ray beam. The assembly was mounted directly in the He flow of the dynamic flux cryostat incorporated into the magnet system.

Figures 2 and 3 show XMCD spectra at the Er $L_{2,3}$ edges for representative points in the phase diagram, and Fig. 4 the corresponding absorption spectra (top panels). The XMCD signal exhibits an obvious evolution of both amplitude and spectral shape as a function of temperature and field, making a direct interpretation of the integral or amplitude of the spectra impossible. In order to elucidate this change in the spectral shape, we have performed a SVD analysis on the entire datasets at each of the L_3 and L_2 edges, respectively.

For the analysis, the dataset is organized in an $(n \times m)$ matrix $\mathbf{A}$ composed of n row vectors of spectra with m data points. The singular value decomposition theorem states that a real $(n \times m)$ matrix $\mathbf{A}$ can be represented as

$$\mathbf{A} = \mathbf{USV}^T, \tag{1}$$

where the left singular $(n \times n)$ matrix $\mathbf{U}$ and the right singular $(m \times m)$ matrix $\mathbf{V}$ are orthogonal, and $\mathbf{S}$ is a $(n \times m)$ diagonal matrix of singular values. The column vectors of $\mathbf{U}$ and $\mathbf{V}$ are the eigenvectors of $\mathbf{AA}^T$ and $\mathbf{A}^T\mathbf{A}$, respectively, and form orthonormal bases. The diagonal elements s_{ii} of $\mathbf{S}$ are the square roots of the eigenvalues of $\mathbf{A}^T\mathbf{A}$, which is n times the variance matrix of the original dataset. The normalized

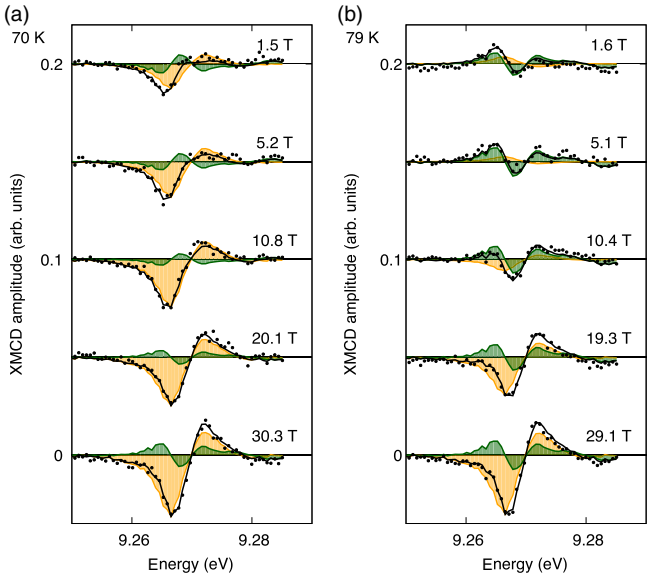

FIG. 3. XMCD at the Er L_2 edge below and above the compensation temperature. (a) 70 K. (b) 79 K. Dots, raw data for selected spectra acquired during the falling part of the field pulse; black line, reconstruction of the data using only the two dominating contributions shown as shaded areas; green, contribution associated with the Fe sublattice; orange, contribution associated with the Er sublattice.

squares of the singular values $s_{ii}^2/tr(\mathbf{S}\mathbf{S}^T)$ therefore quantify the relative contribution of the ith column vector of $\mathbf{V}$ to the variance of the data.

Equation (1) can be interpreted as follows: The column vectors of $\mathbf{V}$ provide a basis to reconstruct the original spectra through multiplication by the coefficients or projections $\mathbf{US}$, with the singular values s_{ii}^2 quantifying the relative importance of a given basis vector for the reconstruction. If the dataset is entirely uncorrelated, all eigenvectors are required for its reconstruction. In a highly correlated dataset, however, considering the hierarchy of the singular values

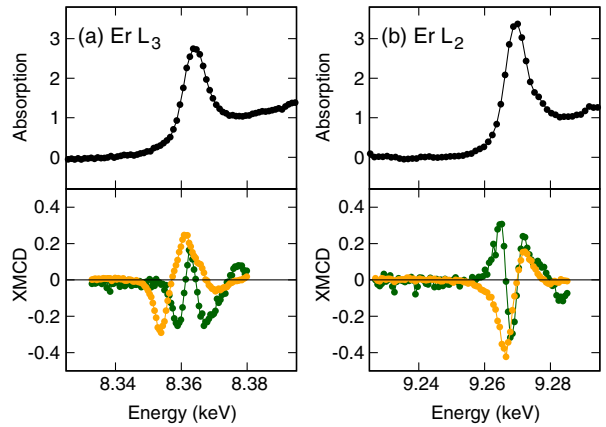

FIG. 4. Absorption spectra and singular value decomposition used for the interpretation of the XMCD data at the Er $L_{2,3}$ edges. (a) Er L_3 edge. (b) Er L_2 edge. Orange, Er-like component; green, Fe-like component. The lines are guides for the eye.

and the shape of the corresponding basis vectors allows one to identify and keep only the relevant spectral components, while discarding those representing mainly noise. This provides us with three important opportunities: First, the hierarchy of singular values allows one to determine the number of independent parameters that can be obtained from the dataset; second, SVD provides an orthonormal basis to reconstruct the spectral shapes; and third, a reconstruction taking only the dominating components into account reduces the noise by exploiting correlations across the dataset. The fundamentals of SVD are found in Ref. [22], and its application to gene expression is discussed in Ref. [23].

We have applied SVD to datasets at the $L_{2,3}$ edges below and above the compensation point. See the Supplemental Material [24] for details on the procedure. At the L_3 edge (L_2 edge) 92.5% (89.5%) of the variance is accounted for by the first two eigenvectors, while all others contribute less than 0.7% (3%) each. In both cases, only the first two eigenvectors shown in Fig. 4 exhibit spectral features beyond noise and are compatible with the energy resolution. It is important to realize, however, that both the singular values and the actual spectral shape of the basis vectors are determined by the composition of the dataset and not by the underlying physics. Any other orthogonal basis and corresponding set of coefficients obtained through rotations $\mathbf{R}$ of the (new reduced) basis and corresponding coefficients are equivalent, and additional knowledge is required to determine appropriate rotations $\mathbf{R}$, so that the eigenvectors represent physical spectra (XMCD), and the coefficients $\mathbf{US}$ meaningful quantities (magnetizations).

In view of the large body of work on the R-T intermetallics and preliminary results on the RIG's, we tentatively assigned the eigenvectors and the field dependence of the coefficients to the Er and Fe sublattices, respectively. In order to determine the appropriate rotation $\mathbf{R}$, we used the knowledge that the Fe-sublattice magnetization is constant and independent of field above the compensation point [17]. Figure 4 shows the resulting basis spectra for rotations of $-2°$ at the Er L_3 edge and 1° at the Er L_2 edge, and Fig. 5 the corresponding field dependences. The shape of the Fe-like spectra is very similar to those reported at the Lu L edges in Ref. [13] for mixed Yb, La, Lu garnet films, while the shape of the Er-like component is similar to those observed in paramagnetic R oxides. In Figs. 2 and 3, the reconstruction using only two components is plotted as a black line along with the original data for selected spectra. The individual contribution of the Er-like (orange) and Fe-like (green) components are shown as shaded areas. Figure 5 shows the coefficients $\mathbf{US}$ for the two components of $\mathbf{V}$ as a function of field for the entire datasets along with simulations using the two sublattice model. For this purpose, the simulations were multiplied by a scaling factor, yet there is only a single scaling for each component and edge for both temperatures. The very good agreement between the Fe signal and the simulation on one side, and with

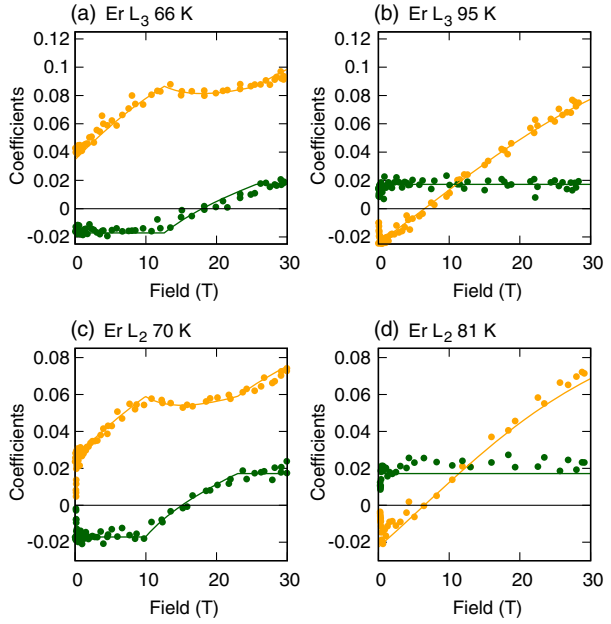

FIG. 5. Field dependence below and above the compensation point. Orange, Er-like component; green, Fe-like component; lines, isotropic two sublattice toy model. (a) Er L_3 edge at 66 K. (b) Er L_3 edge at 95 K. (c) Er L_2 edge at 70 K. (d) Er L_2 edge at 81 K (accidentally very close to the compensation temperature).

previous work [17] on the other side, confirms the working hypothesis that the induced signal follows the net magnetization of the Fe sublattices. The field dependence of the coefficients of the dominating component is also in excellent agreement with simulations of the projection of the Er magnetization on the applied field, and it directly evidences the behavior of the Er sublattices. At high temperatures, where the Fe magnetization dominates, the Er sublattice is at first opposite to the applied field. It gets thermally demagnetized when the latter equals the molecular field and finally increases again along the applied field. Below the compensation point, the Er sublattices dominate and continuously increase until reaching the canted phase, inside of which the Er moments deflect away from the applied field to let the Fe moments pass during their continuous rotation of 180°. We want to point out that the current assignment is phenomenological and based on the assumption that changes in the sublattice magnetizations are much larger than variations in the ratio between spin and orbital contributions. Separating the latter applying sum rules at the R $L_{2,3}$ edges is beyond the scope of this Letter and would require us to identify and remove quadrupolar contributions first. Electronic structure calculations and simulations of XMCD spectra would be desirable for a more detailed understanding.

In conclusion, we measured XMCD at the Er $L_{2,3}$ edges in ferrimagnetic ErIG as a function of field above and below the compensation point. Singular value decomposition was employed to analyze the evolution of both the amplitude and the shape of the energy spectra as a function of temperature and field. The reconstruction of the data at both edges required a base of two spectral components. Using the knowledge that the Fe-sublattice magnetization is field independent above the compensation point and outside of the canted phase [17], we determined a base transformation after which the spectra represent the Er and Fe sublattices, and the field dependence of their amplitudes the sublattice magnetizations. The Er-like component is similar to spectra of paramagnetic rare earth oxides, while the Fe-like contribution has the shape of the induced XMCD signals at the Lu L edges reported for mixed garnet films [13]. The field dependences of the two components are in excellent agreement with a simple isotropic toy model for the sublattice magnetizations and previous work at the Fe K edge [17]. The result illustrates ferrimagnetism on two very different scales: On the one hand, the coupling between the octahedral and tetrahedral Fe sites is so strong that their net magnetization is basically independent of field and temperature, and it rotates by 180° within the canted phase. The Er sublattice, on the other hand, is weakly coupled to the latter. We evidence two characteristic features resulting from this hierarchy of interactions that are not accessible to laboratory methods: (i) the thermal demagnetization and reversal of the Er-sublattice magnetization above the compensation point, and (ii) the deflection of the Er moments away from the direction of the applied field concomitant with the rotation of the iron sublattice in the canted phase below the compensation temperature.

The application of singular value decomposition to obtain information on both the transition metal and rare earth sublattice magnetizations from XMCD at a single absorption edge rationalizes previous approaches in a more general framework and simplifies the exploration of magnetic phase diagrams of the vast class of rare earth–transition metal compounds. In a further application, we have used SVD to study the Ho and Fe sublattices in highly anisotropic $HoFe_5Al_7$ [25], where it was possible to observe both sublattices at either the Fe K or the Ho L_2 and L_3 edges.

C. S. acknowledges the support of the Helmholtz Association through project-oriented funds. We would like to thank M. Krisch for providing single crystals of $Er_3Fe_5O_{12}$, T. Roth for help during early stages of the project, and C. Detlefs for discussion. The experiments would not have been possible without the extensive support of M. Ch. Dominguez and F. Perrin. We acknowledge Quantum Detectors for support with the "ultra system" detector.

*cornelius.strohm@desy.de

[1] L. Néel, Science **174**, 985 (1971).
[2] J. Chaboy, M. A. Laguna-Marco, C. Piquer, H. Maruyama, and N. Kawamura, J. Phys. Condens. Matter **19**, 436225 (2007).

[3] J. Chaboy, M. A. Laguna-Marco, H. Maruyama, N. Ishimatsu, Y. Isohama, and N. Kawamura, Phys. Rev. B **75**, 144405 (2007).
[4] R. Boada, M. A. Laguna-Marco, and J. Chaboy, J. Synchrotron Radiat. **16**, 38 (2009).
[5] R. Boada, M. A. Laguna-Marco, C. Piquer, and J. Chaboy, J. Phys. Condens. Matter **25**, 035604 (2013).
[6] R. Boada, C. Piquer, M. A. Laguna-Marco, and J. Chaboy, Phys. Rev. B **82**, 052407 (2010).
[7] R. Boada, C. Piquer, M. A. Laguna-Marco, and J. Chaboy, Phys. Rev. B **81**, 100404 (2010).
[8] M. A. Laguna-Marco, J. Chaboy, and C. Piquer, Phys. Rev. B **77**, 125132 (2008).
[9] M. A. Laguna-Marco, J. Chaboy, and H. Maruyama, Phys. Rev. B **72**, 094408 (2005).
[10] M. A. Laguna-Marco, J. Chaboy, C. Piquer, H. Maruyama, N. Ishimatsu, N. Kawamura, M. Takagaki, and M. Suzuki, Phys. Rev. B **72**, 052412 (2005).
[11] N. Kawamura, M. Suzuki, H. Maruyama, and T. Ishikawa, J. Synchrotron Radiat. **8**, 425 (2001).
[12] H. Maruyama and N. Kawamura, J. Electron Spectrosc. Relat. Phenom. **136**, 135 (2004).
[13] A. Rogalev, J. Goulon, F. Wilhelm, C. Brouder, A. Yaresko, J. Ben Youssef, and M. V. Indenbom, J. Magn. Magn. Mater. **321**, 3945 (2009).
[14] J. Chaboy, M. A. Laguna-Marco, C. Piquer, R. Boada, H. Maruyama, and N. Kawamura, J. Synchrotron Radiat. **15**, 440 (2008).
[15] A. E. Clark and E. Callen, J. Appl. Phys. **39**, 5972 (1968).
[16] K. Nakao, T. Goto, and N. Miura, J. Magn. Magn. Mater. **54–57**, 1363 (1986).
[17] C. Strohm, T. Roth, C. Detlefs, P. van der Linden, and O. Mathon, Phys. Rev. B **86**, 214421 (2012).
[18] S. Pascarelli, O. Mathon, T. Mairs, I. Kantor, G. Agostini, C. Strohm, S. Pasternak, F. Perrin, G. Berruyer, P. Chappelet, C. Clavel, and M. C. Dominguez, J. Synchrotron Radiat. **23**, 353 (2016).
[19] S. Pizzini, M. Bonfim, F. Baudelet, H. Tolentino, A. San Miguel, K. Mackay, C. Malgrange, M. Hagelstein, and A. Fontaine, J. Synchrotron Radiat. **5**, 1298 (1998).
[20] P. J. E. M. van der Linden, O. Mathon, C. Strohm, and M. Sikora, Rev. Sci. Instrum. **79**, 075104 (2008).
[21] C. Strohm, F. Perrin, M. C. Dominguez, J. Headspith, P. van der Linden, and O. Mathon, J. Synchrotron Radiat. **18**, 224 (2011).
[22] G. H. Golub and C. F. Van Loan, *Matrix Computations*, 4th ed. (Johns Hopkins University Press, Baltimore, 2013).
[23] M. E. Wall, A. Rechtsteiner, and L. M. Rocha, arXiv: physics/0208101.
[24] See Supplemental Material at http://link.aps.org/supplemental/10.1103/PhysRevLett.122.127204 for analysis of x-ray magnetic circular dichroism data using singular value decomposition.
[25] D. I. Gorbunov, C. Strohm, M. S. Henriques, P. van der Linden, B. Pedersen, N. V. Mushnikov, E. V. Rosenfeld, V. Petříček, O. Mathon, J. Wosnitza, and A. V. Andreev, following Letter, Phys. Rev. Lett. **122**, 127205 (2019).